Evaluating the de Hoffmann-Teller cross-shock potential at real collisionless shocks

Steven J Schwartz[1*†], Robert Ergun[1], Harald Kucharek[2], Lynn Wilson III[3], Li-Jen Chen[3], Katherine Goodrich[4], Drew Turner[5], Imogen Gingell[6], Hadi Madanian[7], Daniel Gershman[3], Robert Strangeway[8]

[1]Laboratory for Atmospheric and Space Physics, CU Boulder, Boulder, CO
[2]University of New Hampshire, Durham, NH
[3]Goddard Space Flight Center, Greenbelt, MD
[4]Space Sciences Laboratory, UC Berkeley, Berkeley, CA
[5]Space Exploration Sector, The Johns Hopkins Applied Physics Laboratory, Laurel, MD
[6]Physics and Astronomy, University of Southampton, Southampton, UK
[7]Southwest Research Institute, San Antiono, TX
[8]UCLA, Los Angeles, CA

Key Points:

- Measuring directly the cross-shock de Hoffmann-Teller potential in space is challenging.
- Proposed adaptive frame transformation techniques have limited utility for shocks with 2D or 3D time-varying structure.
- Electron inferences of the potential are robust but assume scattering is negligible.

Manuscript Date 26 Feb 2021; revised 24 May 2021

*Laboratory for Atmospheric and Space Physics, CU Boulder, Boulder, CO
†Also Emeritus Professor, Imperial College London

Corresponding author: Steven Schwartz, steven.schwartz@lasp.colorado.edu

Abstract

Shock waves are common in the heliosphere and beyond. The collisionless nature of most astrophysical plasmas allows for the energy processed by shocks to be partitioned amongst particle sub-populations and electromagnetic fields via physical mechanisms that are not well understood. The electrostatic potential across such shocks is frame dependent. In a frame where the incident bulk velocity is parallel to the magnetic field, the deHoffmann-Teller frame, the potential is linked directly to the ambipolar electric field established by the electron pressure gradient. Thus measuring and understanding this potential solves the electron partition problem, and gives insight into other competing shock processes. Integrating measured electric fields in space is problematic since the measurements can have offsets that change with plasma conditions. The offsets, once integrated, can be as large or larger than the shock potential. Here we exploit the high-quality field and plasma measurements from NASA's Magnetospheric Multiscale mission to attempt this calculation. We investigate recent adaptations of the deHoffmann-Teller frame transformation to include time variability, and conclude that in practice these face difficulties inherent in the 3D time-dependent nature of real shocks by comparison to 1D simulations. Potential estimates based on electron fluid and kinetic analyses provide the most robust measures of the deHoffmann-Teller potential, but with some care direct integration of the electric fields can be made to agree. These results suggest that it will be difficult to independently assess the role of other processes, such as scattering by shock turbulence, in accounting for the electron heating.

Plain Language Summary

Shock waves form when a supersonic flow encounters an immovable object. Thus, ahead of the magnetic bubble formed by the Earth's extended magnetic field, the flow of charged particles emanating from the Sun known as the solar wind is shocked, slowed, and deflected around the Earth. In dense fluids, the conversion of the incident bulk flow energy into heat is accomplished by collisions between particles or molecules. However, the solar wind is so rarefied that such collisions are negligible, and the energy conversion involves more than one kinetic process that couples the different particles to the electromagnetic fields. In particular, electric potentials are believed to control the energy split between positive and negative particles. Measuring electric potentials in space is challenging because there is no available zero "earth" potential. In this work, we explore alternative measurements of the potential associated with the electron physics. Some methods can be made to agree with direct determinations using the measured electrons, but we conclude that despite the unprecedented data quality, they are not sufficient to provide an independent determination of the potential. This poses challenges in assessing other, non-potential physics that also influences the electron energization.

1 Introduction

Shock waves in astrophysical plasma are almost always operating on scales that are much smaller than the particle collisional mean free path. Such collisionless shocks require plasma kinetic processes to decelerate the incident bulk flow and "dissipate" that incident energy flux. These processes operate differently on the different plasma species and electromagnetic fields, and over different scales. They are responsible for preferential heating together with the acceleration to high energies of sub-populations of particles (Kucharek et al., 2003). This unknown partitioning of the incident energy lies at the heart of the shock problem. The bow shock formed by the interaction of the supersonic solar wind flow with the Earth's magnetosphere has long been a prime laboratory for investigating collisionless shock physics thanks to its accessibility by

ever-increasing high quality in situ satellite observations (Burgess & Scholer, 2015; Schwartz, 2006; Schwartz et al., 2013; Krasnoselskikh et al., 2013; Tsurutani & Stone, 1985; Stone & Tsurutani, 1985; Scudder, Mangeney, Lacombe, Harvey, Aggson, et al., 1986).

Feldman et al. (1983) documented the non-Maxwellian nature of electron distributions seen at the bow shock and within the magnetosheath. They showed that the peak of the upstream solar wind distribution was accelerated toward the downstream region and eroded to leave a flat-topped sheath distribution. They noted that the solar wind flow is sub-thermal as far as the electrons are concerned, and established a framework in which electrons traverse, in both directions, a potential at the shock itself. Later work (C. C. Goodrich & Scudder, 1984; Scudder, 1987; Thomsen, Gosling, et al., 1987) pointed out that the potential seen by these electrons is not the same as that which slows down the solar wind ions. In the traditional "Normal Incidence" (NIF) frame, in which the upstream flow is directed along the shock normal, the magnetized electrons drift along the shock surface, giving up energy to the motional $-\mathbf{V} \times \mathbf{B}$ electric field.

de Hoffmann and Teller (1950) employed a different shock frame for their studies of MHD shock waves. This "deHoffmann-Teller" (HT) frame slides along the shock front (to keep the shock at rest) so that the upstream fluid velocity is aligned along the magnetic field. Faraday's Law ensures that this is also the case in the downstream region. The HT frame has been used in studies of shock ion reflection (Sonnerup, 1969; Schwartz et al., 1983), electron "heating" (Scudder, Mangeney, Lacombe, Harvey, Wu, & Anderson, 1986; Thomsen, Mellott, et al., 1987; Schwartz et al., 1988) and magnetopause reconnection (Khrabrov & Sonnerup, 1998; Paschmann et al., 2018) amongst others. Particle energetics are simplified in the HT frame. From the brief discussion above, we see that the energy gained (or lost) by an electron traversing the shock provides a direct measure of the electrostatic potential in the HT frame, so that the electron behavior and HT fields are intrinsically coupled. Establishing the parametric dependence of the HT potential would solve the shock partition problem as far as electron energization is concerned.

Measuring the cross-shock potentials directly is difficult in space due to calibration uncertainties in a floating potential environment, the absence or imbalance of full 3D electric antennae, and other considerations. Attempts to do so are limited (Dimmock et al., 2012; Cohen et al., 2019; Hanson et al., 2019). Electron kinetic observations provide proxy methods to evaluate the HT potential (Scudder, Mangeney, Lacombe, Harvey, Wu, & Anderson, 1986; Schwartz et al., 1988; Lefebvre et al., 2007). These proxies, however, cannot fully disentangle the role of such DC fields in inflating the electron distributions, from the influences of wave-particle scattering (Wilson et al., 2014; Stasiewicz & Eliasson, 2020), magnetic pumping (Lichko & Egedal, 2020) and other processes that have been suggested to play a role in the electron physics. Additionally, 3D global aspects such as curvature (Mitchell & Schwartz, 2013, 2014), and shock ripples (Johlander et al., 2016) can influence the HT potential and electron dynamics. There is a gulf between the idealized 1D steady MHD shocks for which the HT frame was invented, and the dynamic, temporally and spatially varying shocks observed in space.

Comișel et al. (2015), revisited by Marghitu et al. (2017) (hereafter C&M), compared direct integration of the HT potential in a 1D particle in cell simulation with the electron behavior, and concluded that the standard HT transformation by a constant velocity along the shock front resulted in HT potentials that disagreed with that inferred by the electron behavior, being both larger in magnitude and opposite in sign in their simulations. They introduced an "Adaptive Hoffmann-Teller" (AHT) transformation that varied with space through the shock layer in such a way that the local, instantaneous motional electric field vanished. Although this is no longer an inertial

reference frame, the HT potential is linked to the frame invariant parallel electric field and thus might be less sensitive to this non-inertial treatment than the field in other frames of interest. It may be the case, though, that there is variability in the parallel electric field due to waves and fluctuations or temporal variability that requires caution when interpreted in terms of a cross-shock potential. Apart from divergences at nearly perpendicular shocks, the frame transformation velocities are much less than typical electron thermal speeds so that the electron energetics are also relatively insensitive to the frame of reference.

C&M showed that this AHT approach agreed well with the electron determinations of the HT potential profile. This intriguing result opens up the question about whether such an adaptive approach can also work with spacecraft observations of real shocks. We address this question here using the unprecendented high quality field and particle data from NASA's Magnetospheric Multiscale (MMS) mission.

The next sections summarize the data and our primary analysis methods. We then present our Results and provide some Discussion before drawing our final Conclusions.

2 Data

Our primary results are drawn from the Magnetospheric Multiscale mission (MMS) (Burch et al., 2016). We also used data from both the Wind (Harten & Clark, 1995; Wilson et al., 2021) and ARTEMIS (Angelopoulos, 2010) spacecraft to establish the prevailing interplanetary conditions. The main analysis relies on MMS data from the Fast Plasma Investigation (FPI) (Pollock et al., 2016), Fluxgate Magnetometer (FGM) (Russell et al., 2016) and electric field instrumentation (Torbert et al., 2016; Ergun et al., 2016; Lindqvist et al., 2016). We are interested in the quasi-static (DC) electric shock potential. Deducing this from the direct measurement of the 3D electric field ($\mathbf{E}$) by MMS is complicated by a baseline offset which, when integrated, can be as large or larger than the shock potential. The shorter spin-axis sensors contribute a raw baseline offset up to $\sim 3\,\mathrm{mV/m}$ in the plasma conditions we are investigating (Ergun et al., 2016). A small ($< 0.5\,\mathrm{mV/m}$) baseline offset in the spin plane of the spacecraft comes from a sunward-directed electric field due to a small imbalance of photoelectron currents (Lindqvist et al., 2016). These offsets can change if the plasma conditions change. The medium-term (many minutes) electric field offset is routinely removed by a calibration procedure that compares $\mathbf{E}$ to $\mathbf{V}\times\mathbf{B}$ and assumes the median of $\mathbf{E}\cdot\mathbf{B} = 0$ over several minutes. A short-term (4 s) offset correction, such that the median (not average) of $\mathbf{E}\cdot\mathbf{B} = 0$, is applied to $E_\parallel$ to correct for changing plasma conditions. The remaining baseline offsets in $\mathbf{E}$ can be as high as $0.5\,\mathrm{mV/m}$ but are often less. We shall see that one way to represent the shock potential of interest is entirely through $E_\parallel$.

Figure 1 summarizes the configuration of the MMS spacecraft on 2019-03-05. As can be seen in Figure 1b, during this period the spacecraft were co-linear along their common orbit with separations from 100–700 km. They traversed the Earth's bow shock traveling almost exactly along the shock normal. An overview of the plasma observations is given in the left of Figure 2 with a zoomed view spanning ~ 3 min given in Figure 2 (right). The FPI plasma instrumentation is not optimized for measuring the cold solar wind ion beam nor the cool solar wind electrons, which adds both noise and uncertainty to these measurements. The extended disturbed region upstream (later times) of the shock is due to the presence of reflected ions in the shock foot and its extension or reformation, visible after 19:40:00. That reformation structure occurs simultaneously on all four spacecraft (see Figure 1) with systematically growing amplitude. Interestingly, even at MMS1 where this feature is relatively small in magnetic field and density, for example, the electric fields there (panels (i) and (j) of Figure 2)

Table 1. Solar wind and shock parameters

Parameter	Value	Units	Comments
MMS2 Shock Crossing Time	2019-03-05 19:39:05	UT	
MMS2 Location	(10.1, -13.4, 6.85)	GSE R_e	
Upstream field $\mathbf{B}^{up}$	(3.45, 2.47, -2.46)	GSE nT	MMS2 19:43:57–19:44:47
Proton density n_p^{up}	3.5	cm^{-3}	Wind 3DP†
Proton velocity V_p^{up}	(-402, 14, -5)	km/s	Wind 3DP
Proton temperature T_p^{up}	5.9	eV	Wind 3DP
Electron temperature T_e^{up}	4.4	eV	Wind 3DP
Plasma beta β^{up}	0.6		total
Shock normal $\mathbf{n}$	(0.847, -0.482, 0.226)	GSE	(Slavin & Holzer, 1981)
θ_{Bn}	76	deg	
Inflow speed along $\mathbf{n}$: V_n^{up}	-341	km/s	In shock rest frame
Shock Alfvén Mach M_A	6.0		
Fast Magnetosonic Mach M_f	4.9		
Spacecraft separations:			$\mathbf{r}_{21} \equiv \mathbf{r}_1 - \mathbf{r}_2$, etc.
$\mathbf{r}_{21} \cdot \mathbf{n}$	-201	km	
$\mathbf{r}_{14} \cdot \mathbf{n}$	-104	km	
$\mathbf{r}_{43} \cdot \mathbf{n}$	-407	km	
Shock motion along $\mathbf{n}$:			$\mathbf{r}_{21} \cdot \mathbf{n}/(t_1 - t_2)$, etc.
$V_{n,2\to1}^{sh}$	-7.4	km/s	
$V_{n,1\to4}^{sh}$	-7.8	km/s	
$V_{n,4\to3}^{sh}$	-1.3	km/s	First encounter

†All Wind parameters are 20 minute averages lagged 65 minutes.

are comparable in amplitude to that at the main shock ramp at 19:39:30 (cf. Wilson et al. (2014)).

Table 1 summarizes the underlying solar wind conditions and derived shock parameters. We have drawn on solar wind data from the Wind spacecraft, lagged by 65 minutes from Wind's upstream location to the nose of the bow shock. In view of its critical role in our analysis, we use a local MMS measurement to characterize the upstream magnetic field, which is within 7 degrees of that observed by Wind. We use an emperical shock model (Slavin & Holzer, 1981; Schwartz, 1998) to determine the direction of the shock normal.

The times of the shock crossing at the different spacecraft are indicated by the vertical dashed lines in Figure 1d-g, which intersect the mid-points of the full shock ramp field profiles. MMS3 (Figure 1g) exited the magnetosheath briefly as the shock motion stalled and reversed, before a final exit at 19:45. Table 1 shows that the derived shock speed along the normal was almost the same between the first ($2 \to 1$) and second ($1 \to 4$) spacecraft pairs before slowing down as MMS3 encountered it. In our analysis we will draw primarily on data from MMS1 during the middle of the nearly constant shock motion.

3 Background and methodology

3.1 Shock reference frames

We review the subject of electric fields at a shock here. We employ the standard 1D shock lmn coordinates in which the shock normal $\mathbf{n}$ points into the upstream (unshocked) region, the upstream magnetic field $\mathbf{B}^{up}$ lies in the ln plane with $B_l^{up} > 0$,

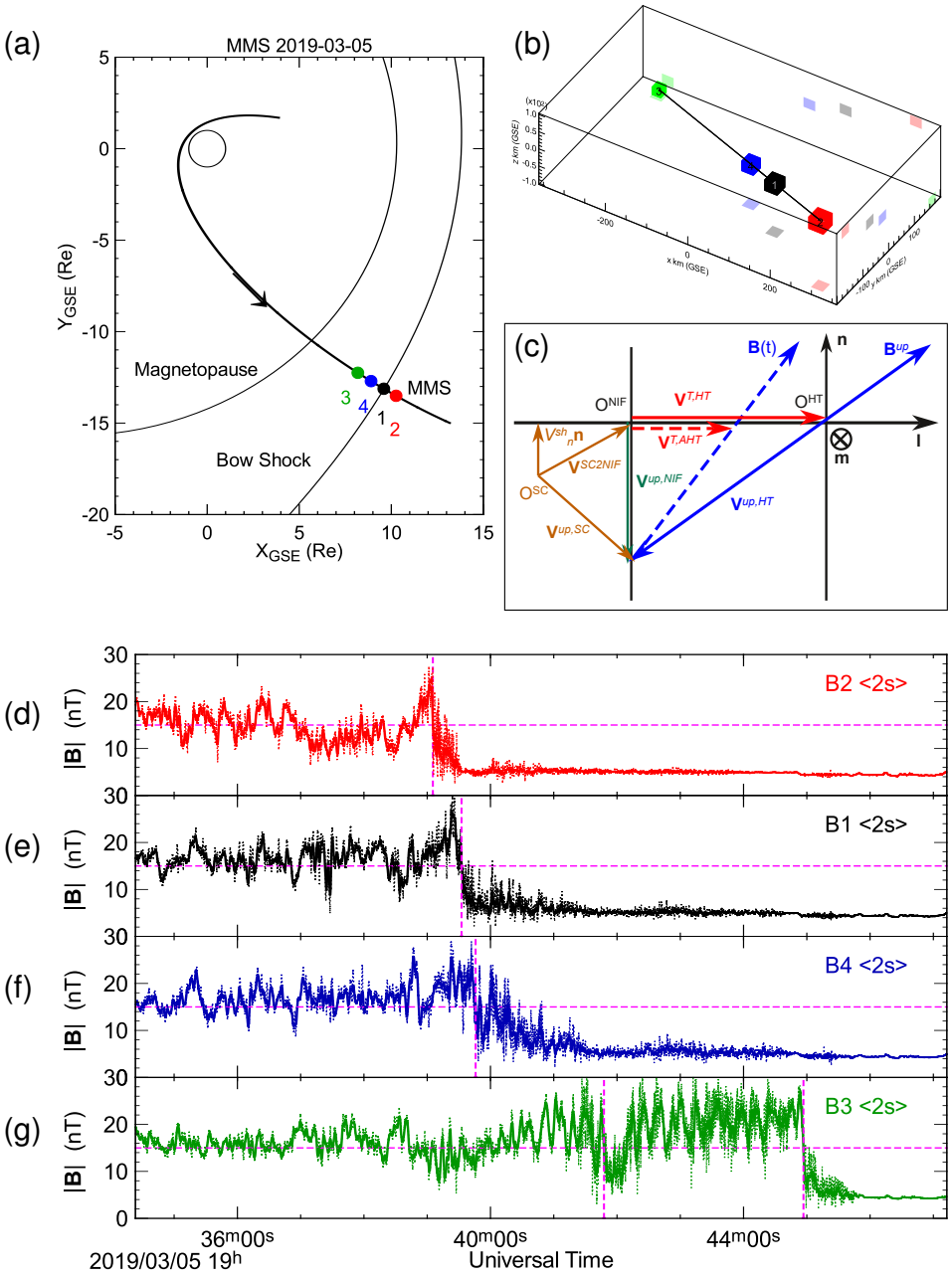

Figure 1. Configuration of MMS on 2019-03-05. (a) MMS orbit outbound through the bow shock, showing the relative positions of MMS1-4. (b) Detailed relative positions of the four MMS spacecraft, showing their co-linear alignment which is along the orbit and therefore, from (a) essentially along the shock normal. (c) Velocity space diagram of the coordinate systems, velocities and transformation velocities illustrating their use (see text). (d)-(g) Magnetic field magnitudes measured by the four spacecraft (dotted = full resolution; solid = 2 s averages). The times corresponding to the mid-point of the shock ramps are located by the intersections of the dashed horizontal and vertical lines in each panel. MMS3 (g) exited the magnetosheath briefly at $\sim 19:41:48$ and for the second time at $\sim 19:44:56$.

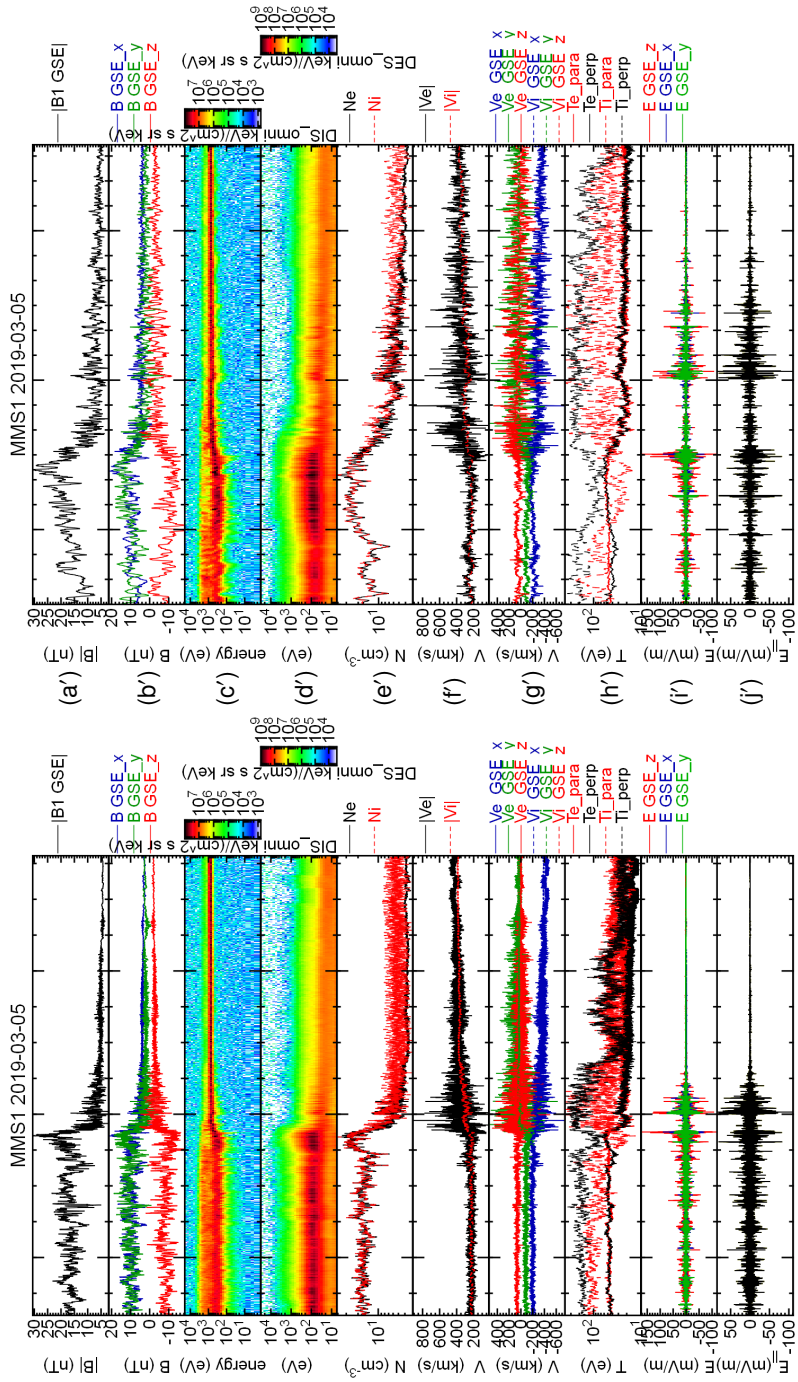

Figure 2. Overview (L) and detail (R) of the shock crossing by MMS on 2019-03-05 used in this study. All data are from MMS1 and taken in burst mode. (a),(b) magnetic field magnitude and components (c), (d) ion and electron omni-directional energy spectra (e) electron and ion number densities (f), (g) ion and electron bulk velocity magnitudes and components (h) electron (solid) and ion (dashed) temperatures along (red) and perpendicular (black) to the local magnetic field (i) DC electrid field components and (j) DC field $E_{||}$ along the magnetic field.

and $\mathbf{m}$ completes the right-handed system as sketched in Figure 1c. For steady 1D shocks, the downstream field should also lie in the ln plane, and in both NIF and HT frames the normal, field and bulk flow velocities up- and downstream are coplanar. In the NIF frame, the motional $-\mathbf{V}\times\mathbf{B}$ electric field is along $+\mathbf{m}$ and, in steady-state applications, is spatially uniform.

A word about notation. In the derivations below, we use subscripts to denote component and species labels. Superscripts are reserved for descriptive labeling and reference frame designation. We will consider transformations into different frames (HT, NIF, etc.) and use a superscript "α" to denote a non-specified frame, which will be identified elsewhere, e.g., α =HT. Frame transformations generally involve a velocity shift that relates the fields in one frame to those in another, e.g., as illustrated in Figure 1c. We denote by a superscript "T" any quantity that is used to specify or calculate that velocity shift, so that, for example, $\mathbf{V}^{T,HT}$ is the velocity shift required to move into the HT frame. Although it is possible to transform directly between any two frames, e.g., from the spacecraft frame to the HT frame, for ease of use, unless otherwise stated we start in the NIF frame. The necessary transformation into the NIF frame is given below. Finally, we will see, following C&M, that it is also convenient to represent a frame transformation by a transformation electric field $\mathbf{E}^{T,\alpha}$ that can be used to calculate $\mathbf{V}^{T,\alpha}$. Depending on the frame, $\mathbf{E}^{T,\alpha}$ may or may not correspond to an electric field that would be measured in a particular frame. Thus $\mathbf{E}^{T,\alpha}$ is the transformation electric field employed in calculating the velocity shift $\mathbf{V}^{T,\alpha}$ to move into the α frame, and $\mathbf{E}^{\alpha}$ is the electric field measured in that α frame.

Collisionless particle motion is controlled by electromagnetic fields that are self-consistent with the particle charge density and currents. However, the electric field is not invariant under Gallilean transformation, and so analysis must specify the frame of reference being used. Although the classic shock in a collisional fluid is usually analyzed in the Normal Incidence Frame (NIF), in which the shock is at rest and the incident bulk flow is directed along the shock normal, de Hoffmann and Teller (1950) noticed that in a magnetized plasma there are benefits to transforming to a frame in which the bulk flow is directed along the magnetic field. Faraday's Law ensures that in this frame this will be true in both the upstream and downstream regions, as the m-component of $\mathbf{E}$ is zero and continuous. In this deHoffmann-Teller (HT) frame, the motional $-\mathbf{V}\times\mathbf{B}$ electric field vanishes, which makes particle motion and energetics particularly simple. It has been employed in studies of particle energization at shocks (Sonnerup, 1969; Thomsen et al., 1983; Schwartz et al., 1983; Wu, 1984), in electron heating at shocks (Scudder, Mangeney, Lacombe, Harvey, Aggson, et al., 1986; Thomsen, Mellott, et al., 1987; Schwartz et al., 1988; Lefebvre et al., 2007), and plays a central role in other phenomena, such as magnetic reconnection (Khrabrov & Sonnerup, 1998).

3.2 Shock electric fields

In the HT frame at steady 1D shocks, the only electric field is within the shock layer itself, directed outward along the shock normal, and is intimately related to the electron fluid behavior. This can be established by solving the electron momentum equation for the electric field $\mathbf{E}^{ve}$ in the electron fluid frame given the field $\mathbf{E}$ and flow velocities in an arbitrary frame:

$$\mathbf{E}^{ve}\equiv\mathbf{E}+\mathbf{V}_e\times\mathbf{B}=-\frac{1}{en_e}\nabla\cdot\underline{\underline{\mathbf{P}}}_e+\text{inertial and frictional terms} \tag{1}$$

The leading term, $\frac{1}{en_e}\nabla\cdot\underline{\underline{\mathbf{P}}}_e$ on the right hand side of Equation 1, when defined in the electron fluid rest frame, is the frame invariant ambipolar electric field $\mathbf{E}^{amb}$. If we evaluate Equation 1 in the HT shock rest frame, $\mathbf{E}^{ve}\rightarrow\mathbf{E}^{HT}$ since $\mathbf{V}_e\parallel\mathbf{B}$. Looking at the right hand side, we see, that this field $\mathbf{E}^{HT}$, determined by the divergence of the

electron pressure, is directed along the shock normal since the off-diagonal terms of the pressure tensor, together with the inertial terms, are typically much smaller than the diagonal terms.

Within the shock layer, the electron bulk flow velocity $\mathbf{V}_e$ drifts in the m-direction relative to that of the ions, but stays nearly parallel to the magnetic field in the HT frame (Scudder, 1987). That drift, however, when viewed in the NIF frame, is along the upstream motional electric field and results in the electron NIF energization being substantially less than the ion energy loss to the NIF cross-shock potential (C. C. Goodrich & Scudder, 1984).

It is also possible to project the electric field along the magnetic field by dotting Equation 1 with a unit vector along $\mathbf{B}$.

$$E_{\parallel} = -\frac{1}{en_e}\left(\nabla \cdot \underline{\underline{\mathbf{P}}}_e\right) \cdot \mathbf{B}/B \tag{2}$$

Since $\mathbf{E} \cdot \mathbf{B}$ is frame invariant, $E_{\parallel}$ in Equation 2 is frame invariant, which can also be confirmed by its dependence only on the electron pressure divergence. Comparing Equation 2 with the ambipolar field on the right hand side of Equation 1, which we argued above is directed along the shock normal, we can re-write $\mathbf{E}^{amb}$ explicitly as:

$$\mathbf{E}^{amb} = -\frac{\mathbf{n}}{en_e}\left(\nabla \cdot \underline{\underline{\mathbf{P}}}_e\right) \cdot \mathbf{B}/B_n \tag{3}$$

3.3 Transforming to the HT frame

The transformation velocity $\mathbf{V}^{T,\alpha}$ from a shock rest frame into the HT frame is found by finding the frame in which the flow and field are aligned, or equivalently in which the components of the motional $\mathbf{E}$ tangential to the shock vanish. C&M do this by looking at the specific E_l and E_m expressions under frame transformation. These considerations can be encapsulated in the following compact form:

$$\mathbf{V}^{T,\alpha} = -\mathbf{n} \times \mathbf{E}^{T,\alpha}/B_n^{T,\alpha} \tag{4}$$

where we remind the reader that we have used the superscript "T, α" to denote parameters associated with the transformation to the α-frame in anticipation of the possible alternatives developed below. Interestingly, this formulation of $\mathbf{V}^{T,\alpha}$, with $\mathbf{E}^{T,\alpha}$ set to the measured field $\mathbf{E}$ in an arbitrary frame, will yield an electric field $\mathbf{E}^{\alpha} = \mathbf{E} + \mathbf{V}^{T,\alpha} \times \mathbf{B}$ that is associated with the frame invariant ambipolar field regardless of the initial frame of reference. However, since by construction $\mathbf{V}^{T,\alpha}$ is perpendicular to the shock normal $\mathbf{n}$, it will only transform to the origin of the HT frame if the shock is at rest in the initial frame (see, e.g., Figure 1c).

Equation 4 is the heart of our formalism. Below we illustrate its use in the standard HT transformation as well as different adaptive attempts to generalise the transformation in the case of non-steady and spatially varying fields. Figure 1c illustrates the different vectors and frames used in the remainder of the paper, showing in particular how the transformation to the HT frame derived in the next section is accomplished. For convenience, Figure 1c is sketched in 2D, e.g., in the NIF nl plane. In practice, the spacecraft origin and associated vectors (colored brown in the figure), instantaneous $\mathbf{B}(t)$ and adaptive transformation velocity $\mathbf{V}^{T,AHT}$ will typically have components in the $\mathbf{m}$ direction, which is into the plane of Figure 1c.

3.4 Spacecraft to NIF to HT frame

Although it is both possible and practical to transform fields directly from the spacecraft frame of reference to the HT frame and its adapted variants, in expositions

below we start from the NIF frame, which moves relative to the spacecraft frame at a velocity

$$\begin{aligned}\mathbf{V}^{SC2NIF} &= V_n^{sh}\mathbf{n} + \mathbf{n}\times\left(\mathbf{V}^{up,SC}\times\mathbf{n}\right)\\ &= V_n^{sh}\mathbf{n} + \mathbf{V}^{up,SC} - \mathbf{n}\left(\mathbf{V}^{up,SC}\cdot\mathbf{n}\right)\end{aligned} \tag{5}$$

where V_n^{sh} is the signed shock velocity relative to the spacecraft along the shock normal, and $\mathbf{V}^{up,SC}$ is the constant upstream ("*up*") flow velocity measured in the spacecraft frame (see Figure 1c). From (5) we see that the upstream flow velocity in the NIF frame is purely along the shock normal, since

$$\begin{aligned}\mathbf{V}^{up,NIF} &= \mathbf{V}^{up,SC} - \mathbf{V}^{SC2NIF}\\ &= \mathbf{V}^{up,SC} - V_n^{sh}\mathbf{n} - \mathbf{V}^{up,SC} + \mathbf{n}\left(\mathbf{V}^{up,SC}\cdot\mathbf{n}\right)\\ &\equiv V_n^{up}\mathbf{n}\end{aligned} \tag{6}$$

where V_n^{up} is the signed component of the upstream flow velocity along the shock normal in the NIF, or any other, shock rest frame. We then find the NIF electric field as

$$\mathbf{E}^{NIF} = \mathbf{E}^{SC} + \mathbf{V}^{SC2NIF}\times\mathbf{B} \tag{7}$$

Starting from the NIF frame, the electric field in the α-frame following transformation using $\mathbf{V}^{T,\alpha}$ from (4) is

$$\mathbf{E}^{\alpha}(t) = \mathbf{E}^{NIF}(t) + \mathbf{V}^{T,\alpha}\times\mathbf{B}(t) \tag{8}$$

$$= \mathbf{E}^{NIF}(t) - \left(\mathbf{n}\times\mathbf{E}^{T,\alpha}/B_n^{T,\alpha}\right)\times\mathbf{B}(t) \tag{9}$$

$$= \mathbf{E}^{NIF}(t) - \mathbf{E}^{T,\alpha}B_n(t)/B_n^{T,\alpha} + \mathbf{n}\left(\mathbf{E}^{T,\alpha}\cdot\mathbf{B}(t)\right)/B_n^{T,\alpha} \tag{10}$$

where we have shown the time dependence as a shorthand for both spatial and temporal dependencies of the fields. In the adaptive forms introduced by C&M, some of the ingredients in $\mathbf{V}^{T,\alpha}$ are also not constant. We shall assume throughout that the shock normal $\mathbf{n}$ is constant (see Section 5).

3.5 Standard HT transformation

In general, the action of the middle term in Equation 10 attempts primarily to cancel out the NIF tangential field components. The field along $\mathbf{n}$ involves all three terms to some extent. So, for example, the traditional transformation from the NIF frame to the HT uses constant upstream values for the transformation, i.e. $\mathbf{E}^{T,HT} = -\mathbf{V}^{up}\times\mathbf{B}$. Noting that in the NIF frame $\mathbf{V}^{up}$ has only an $\mathbf{n}$ component, this yields

$$\mathbf{E}^{T,HT} = -V_n^{up}\mathbf{n}\times\mathbf{B}^{up} \quad \text{with} \quad B_n^{T,HT} = B_n^{up} \tag{11}$$

$$\mathbf{V}^{T,HT} = +\mathbf{n}\times\left(V_n^{up}\mathbf{n}\times\mathbf{B}^{up}\right)/B_n^{up} \tag{12}$$

$$\mathbf{E}^{HT} = \mathbf{E}^{NIF}(t) + V_n^{up}\mathbf{n}\times\mathbf{B}^{up}\frac{B_n(t)}{B_n^{up}} - \mathbf{n}\left(V_n^{up}\mathbf{n}\times\mathbf{B}^{up}\right)\cdot\mathbf{B}(t)/B_n^{up} \tag{13}$$

For strictly 1D shocks, B_n is constant in space and time, so the fraction in the middle term of Equation 13 is unity. This term then cancels the NIF upstream tangential (m-component) electric field. From the last term we see that the normal component of $\mathbf{E}^{HT}$ is the same as that in the NIF frame unless the local magnetic field has a non-zero component along this $\mathbf{m}\equiv\mathbf{n}\times\mathbf{l}$ direction. This role of non-coplanar magnetic fields within the shock layer in making the cross-shock electric fields, and hence potentials, different in the HT and NIF frames is at the heart of this subject (C. C. Goodrich & Scudder, 1984; Thomsen, Gosling, et al., 1987).

3.6 Adaptive HT transformations

C&M introduced an adaptive approach which followed variations of the fields by using a non-constant local frame transformation to remove the tangential electric field at every point. In the simple case of constant flow velocity, this is equivalent to letting the HT origin in Figure 1c move horizontally (i.e., in the lm-plane), to keep the shock at rest and to follow the variations in $\mathbf{B}(t)$. This prescription ensures that the flow velocity stays aligned with $\mathbf{B}$. The red-dashed arrow labelled $\mathbf{V}^{T,AHT}$ shown in Figure 1c illustrates this simple case. The formalism developed by C&M and used here uses the measured electric field in $\mathbf{E}^{T,AHT}$ (Equation 14 below) and thus implicitly follows variations in the motional $-\mathbf{V}\times\mathbf{B}$ field that are generated by any variations in the flow velocity as well as variations in $\mathbf{B}$.

C&M's method (see Marghitu et al. (2017) Equation 5b) in our framework simply uses the local electric field $\mathbf{E}^{NIF}(t)$ in the NIF frame as the transforming electric field $\mathbf{E}^{T,\alpha}$ in Equation 4, which yields the following set of relations:

$$\mathbf{E}^{T,AHT} = \mathbf{E}^{NIF}(t) \quad \text{with} \quad B_n^{T,AHT} = B_n^{up} \tag{14}$$

$$\mathbf{V}^{T,AHT}(t) = -\mathbf{n}\times\mathbf{E}^{NIF}(t)/B_n^{up} \tag{15}$$

$$\mathbf{E}^{AHT} = \mathbf{E}^{NIF}(t)\left(1-\frac{B_n(t)}{B_n^{up}}\right) + \mathbf{n}\left(\mathbf{E}^{NIF}(t)\cdot\mathbf{B}(t)\right)/B_n^{up} \tag{16}$$

In the 1D case applicable to C&M's simulations the first term in Equation (16) vanishes leaving $\mathbf{E}^{AHT}$ with only a normal component related explicitly to the frame-invariant parallel electric field as it should. In the 2D and 3D case, where the magnetic field component along the (assumed) constant normal direction varies, Equation (16) shows that not only is that cancellation of the tangential electric field in the first term imperfect, but that there can also be an influence on the normal component E_n^{AHT} from this term that can be significant and of varying sign depending on the instantaneous $B_n(t)$. We shall see later that this influence and related considerations suggest that seeking an appropriate frame transformation velocity of any kind is less satisfactory than methods which either use proxies for the electric field in the HT frame, or which focus from the outset on the parallel electric field directly.

The formal cancellation problem can be alleviated by extending the AHT to use the full time/space dependent fields. Simply insert $B_n(t)$, in the frame transformation specification (Equations (14)–(15)) in place of the constant B_n^{up} in those equations, and hence in Equation (16). We call this the "AHTt" transformation. It solves the tangential field problem at the expense of making $\mathbf{E}^{AHTt}$ proportional to $1/B_n(t)$ which, unlike the 1D case, can lead to singularities:

$$\mathbf{E}^{AHTt} = \mathbf{n}\left(\mathbf{E}^{NIF}(t)\cdot\mathbf{B}(t)\right)/B_n(t) \tag{17}$$

3.7 Shock potentials

Armed with estimators $\mathbf{E}^{\alpha}$ of the electric field in the HT frame (e.g., α = HT, AHT, AHTt), the potential profile in the HT frame can be found by integration through the shock layer:

$$\phi^{\alpha}(n) = -\int^{n} E_n^{\alpha}(t)\,dn = -\int^{s_\parallel} E_\parallel^{\alpha}(t)\,ds_\parallel \tag{18}$$

where n and $s_\parallel$ are coordinates along the shock normal and magnetic field respectively. We use the multiple spacecraft observations to determine the shock velocity V_n^{sh}, assumed to be constant, along the normal relative to the spacecraft. This enables us to write $dn = -V_n^{sh}\,dt$ and hence we evaluate the potential profile

$$\phi^{\alpha}(t) = V_n^{sh}\int_{t_o}^{t} E_n^{\alpha}(t)\,dt \tag{19}$$

up to some arbitrary constant.

C&M evaluated the standard ϕ^{HT} directly from the electric fields in their simulations based on these steady state formulations and found that it gave poor agreement with the electron behavior, even to the extent of implying the electrons should deflate ("cool") in their simulation instead of the observed inflation. Although there can be significant differences between the electric fields in simulations vs. nature (Wilson et al., 2021) the electron behavior should always be self-consistent with the fields in both cases. They cross-checked the electron response by Liouville mapping the electron distributions (Scudder, Mangeney, Lacombe, Harvey, Wu, & Anderson, 1986; Lefebvre et al., 2007; Schwartz et al., 1988), and also calculated the integrated ambipolar field directly.

The adaptive extension of HT analysis to time-varying systems worked well in the simulations reported by C&M. However, careful inspection of the derivation shown here reveals that the application to 2D or 3D time-variable shocks is both unclear and danger-ridden. In the 1D case, both the shock normal $\mathbf{n}$ and, thanks to $\nabla \cdot \mathbf{B} = 0$, the normal component of the magnetic field B_n are constants. In 2D or 3D, allowing B_n to vary in time opens up the possibility for incomplete cancellation of $\mathbf{E}^{NIF}$ in Equation (16) or large jumps in $\phi^{AHTt}(t)$ whenever the local B_n passes through or close to zero. We have not found an approach that enables $\mathbf{n}(t)$ to be determined, nor is there any guarantee that B_n would be better behaved if we did. Below we compare the various estimators of ϕ using high quality in situ spacecraft data. None of these methods overcomes the intrinsic difficulty of measuring DC-coupled electric fields in space over the scales of a shock traversal.

3.8 Electron behavior

For nearly all shocks in the heliosphere, the bulk flow velocities, together with the shock velocities, are much smaller than the electron thermal speeds. In the absence of collisions, electrons travel along the field lines in both directions across the shock. Those traveling into the shock from the upstream (unshocked) side get accelerated by the HT potential while those traveling away from the shock get decelerated. This leads to electron distributions that are "inflated", (Scudder, Mangeney, Lacombe, Harvey, Wu, & Anderson, 1986; Scudder, 1995) i.e., broader - in both directions - in the downstream region than in the upstream one, giving the impression that the electrons are heated from upstream to downstream. While this is the consequence at the fluid level, it is clear that the collisionless particle behavior is more subtle.

The inflation of electron phase space is linked to the HT cross-shock potential, ϕ^{HT}, which is found by integrating $\mathbf{E}^{HT}$ across the shock. In a shock rest frame this potential will be path independent, and can be found by integrating, e.g., along the shock normal. A magnetized electron will follow the field line, and its energization is equivalent to integrating the parallel projection of $\mathbf{E}$ along the field line. It is important to recall that the bulk flow velocity is small compared to the electron thermal speed. Electrons from the downstream region can overcome the potential and lose kinetic energy as they emerge to stream upstream away from the shock.

We exploit the electron single particle behavior described above to calculate $\phi^{Liouville}$ using Liouville's Theorem. We perform this by transforming the electron distribution functions into the steady-state HT frame based on upstream plasma parameters. We approximate the distribution $f(v_\parallel, v_\perp = 0)$ at zero magnetic moment by averaging over a range of pitch angles within 30° of the ± magnetic field direction. We average the resulting distribution function $f(v_\parallel)$ within the upstream region to use as a reference distribution $f^{ref}(v_\parallel)$, that we then represent by fitting a κ-distribution. For each measured $f(v_\parallel, t)$ we find the local $\phi(t)$ that minimizes the least squares difference between f^{ref} shifted by an energy $e\phi(t)$ and the measured ones over a range

of values of f that correspond to being close to but beyond the edge of the downstream flattopped distribution. We do this separately for electrons traveling parallel to the magnetic field, corresponding in our example to electrons traveling upstream, and anti-parallel electrons.

Note that this procedure maps incoming electron trajectories forward in time and outgoing electrons backward in time from the f^{ref} to $f(v_\parallel, t)$. Technically, Liouville's theorem requires following each electron trajectory to other points on that same trajectory. In addition to time-variability, those trajectories also drift tangentially along the shock surface (C. C. Goodrich & Scudder, 1984). We assume here that the distributions are quasi-steady in time and space in order to use a snapshot of the upstream distribution to map to all other locations and times. We assume that the electrons conserve their first adiabatic invariant, namely their magnetic moments μ_m. We focus on field-aligned electrons with $\mu_m = 0$ as this removes dependency on the magnetic profile.

One example of this procedure is shown in Figure 3 below. The blue f_κ curves are fits to the upstream averaged reference distribution drawn in green. The reference interval is delineated by magenta dashed lines in the bottom panel. We shift those blue κ-fits by an energy $e\phi$. Considering only the values of $f(v_\parallel)$ within the dashed horizontal mapping limits, we find the value of ϕ that makes the shifted distribution best match the red observed distribution $f_{obs}(v_\parallel, t)$. The shifted f_{mapped} distributions are shown in red.

The effect of the HT velocity transformation can be seen in the asymmetry at low energies and by the steeper (shallower) $f(v)$ in the anti-parallel (parallel) direction. Phase space densities above the flat-top values in the anti-parallel direction are probably also contaminated by secondary or photoelectrons of spacecraft origin. The mapped distributions (black) fit the parallel (upstream or sunward) electron distribution well. The anti-parallel (incoming) mapping fit is poorer. It is not clear if this can be attributed to the uncertainties in or influence of the HT transformation, or if other energization mechanisms operate specifically on the incoming (anti-parallel) electron population. The lower panel of Figure 3 shows $\phi^{Liouville}$ for the separate populations and the locations of the reference distribution (magenta interval) and the example instance used in the top panel. Generally, the anti-parallel $\phi^{Liouville}$ is noisier, although both potentials agree well through the main shock ramp. The Liouville mapping estimator for ϕ is unique in that it does not require an explicit spatial integral and thus is immune to errors in determination of the shock speed.

3.9 Summary of ϕ^{HT} estimators

The analysis and derivations performed in the previous sub-sections lead to a number of possible estimations of the cross-shock de Hoffmann-Teller potential. We employ several alternatives for illustration and comparison purposes. Specifically, we calculate:

1. $\phi^{HT} = V_n^{sh} \int E_n^{HT}(t)\, dt \equiv V_n^{sh} \int \left(\mathbf{E}^{NIF}(t) + \mathbf{V}^{T,HT} \times \mathbf{B}^{up}\right) \cdot \mathbf{n}\, dt$
   using Equation (11) or (12). This is the traditional method using static upstream values for the (constant) frame transformation velocity.
2. $\phi^{AHT} = V_n^{sh} \int \left(\mathbf{E}^{NIF}(t) + \mathbf{V}^{T,AHT}(t) \times \mathbf{B}(t)\right) \cdot \mathbf{n}\, dt$
   using Equation (14) or (15). This is the conservative application of C&M's adaptive de Hoffmann-Teller transformation, with a time dependent transformation velocity but retaining $B_n =$ constant.
3. $\phi^{AHTt} = V_n^{sh} \int \left(\mathbf{E}^{NIF}(t) + \mathbf{V}^{T,AHTt}(t) \times \mathbf{B}(t)\right) \cdot \mathbf{n}\, dt$
   which is the full naïve application of the adaptive transformation that uses $B_n(t)$ in the frame transformation to reach Equation (17).

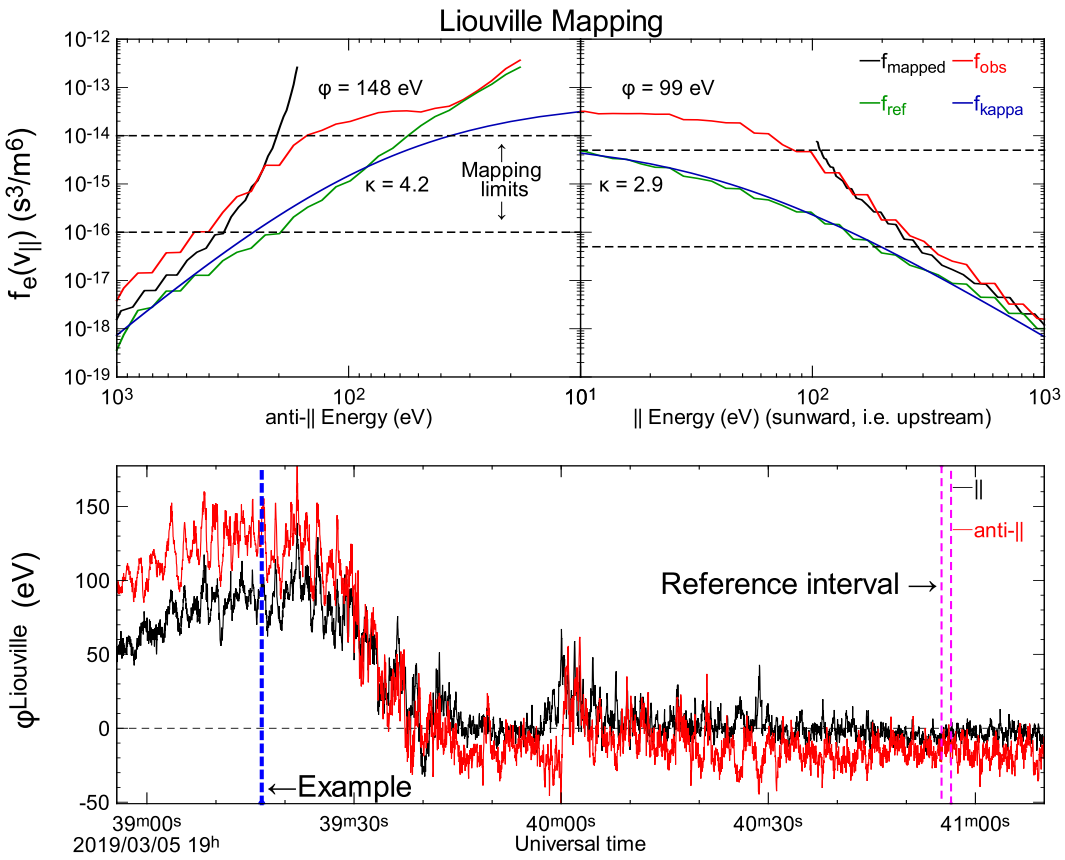

Figure 3. Illustration of the Liouville mapping determination of the deHoffmann-Teller potential. The top panel shows the reference distribution (green) which is an average of electrons travelling with pitch angles in the range $0 - 30^\circ$ or $150 - 180^\circ$ over the interval delineated by the magenta dashed lines in the lower panel. The blue curves show the κ-distribution fits to those reference distributions. The least squares method of mapping within the dashed mapping limits result in a shift of the reference distributon to the black f_{mapped}. This example was drawn from the time downstream of the shock overshoot indicated by the dashed blue line in the bottom panel. The bottom panel shows the time series of $\phi(t)$ determined by repeating this process for all times separately for electrons within 30° of being field-aligned (black) and anti-parallel (red). All data are drawn from MMS1.

4. $\phi^{\parallel} = -\int E_{\parallel}(t)\, ds_{\parallel} \equiv V_n^{sh} \int E_{\parallel}(t) B^{up}/B_n^{up}\, dt$
   which is a direct integration (see Equation (18)) of the special $E_{\parallel}(t)$ data product provided by the electric fields instrument team. This does not require the calculation of a frame transformation thanks to the frame invariance of $E_{\parallel}$. However, we employ static upstream fields and a determination of the shock normal velocity V_n^{sh} in the spacecraft frame to convert from dn to $ds_{\parallel}$. This enables a direct comparison with ϕ^{HT}. Additionally, this calculation does not require any down-sampling of the electric field to the cadence of other measurements.
5. $\phi^{ve} = V_n^{sh} \int (\mathbf{E}(t) + \mathbf{V}_e(t) \times \mathbf{B}(t)) \cdot \mathbf{n}\, dt$
   which integrates the left hand side of the electron momentum equation (1). Despite the fact that this is the electric field in the electron frame rather than a shock rest frame, it is equivalent to the ambipolar $\mathbf{E}^{amb}$ from equation (3) and hence can be integrated to estimate ϕ^{HT}. In essence, it removes all the contributions to the motional electric field, including those along the shock normal direction. Unlike the various forms using $V^{T,\alpha}$, ϕ^{ve} integrates quantities measured in the spacecraft frame without any additional frame transformations.
6. $\phi^{amb} = \int \dfrac{1}{en_e} \dfrac{dP_{e,nn}}{dt}\, dt$
   which is a direct integration of the right hand side of the electron momentum equation (1) again assuming that the diagonal pressure term dominates. Note that the shock velocity does not appear here as the spatial integration of the weighted spatial derivative of $P_{e,nn}$ is converted directly into the time domain.
7. ϕ^{Lvl0},
   the Liouville-mapped determination of ϕ as described in the preceding section and illustrated in Figure 3. We use the parallel rather than anti-parallel estimator as discussed in relation to Figure 3. Unlike the other estimators of ϕ, ϕ^{Lvl0} is not the result of an integration; it provides the absolute potential relative to the location of the reference $f^{ref}(v_{||})$.

4 Results

In this section we apply these concepts to the data taken by MMS as summarized in Figure 2 and Table 1. Figure 4 shows all the estimators discussed in the preceding section. The ambipolar and Liouville-mapped potentials (ϕ^{amb} and ϕ^{Lvl0}) agree well with one another. This is not surprising as they both are proxies for the overall inflation of $f(v)$, although the very detailed match seen in panel (e) is perhaps not guaranteed given that one is an integral. These two electron-based potentials provide the standard against which all the other forms involving electric field measurements should be tested (Comişel et al., 2015; Marghitu et al., 2017). For all integrated potentials, we choose a common point at the base of the shock ramp ($t \sim 19:39:43$) to be $\phi = 0$. Several of the potentials drift away from being constant farther upstream or downstream. This drift could be indicative of small offsets in the measured fields, as discussed further below. There is no a priori reason for such offsets to be constant across the entire interval under investigation.

We preface this section with a note of caution. It is not possible to separate completely the limitations of approaches that employ the DC electric field measurements for the HT transformation velocities and resulting integrations of those fields from the uncertainties related to the measurement and calibration of the fields themselves.

Panel (b) of Figure 4 reveals that the fully time-dependent extension of the adaptive HT concepts developed by C&M results in large discrete steps in the integrated potential ϕ^{AHTt} (magenta curve). Much of this curve extends beyond the limits of the panel. These steps can be traced to locations where the normal component $B_n(t)$ of the magnetic field approaches or passes through zero. At these locations, the adaptive HT transformation velocity (Equation (15) with B_n^{up} replaced by $B_n(t)$) becomes

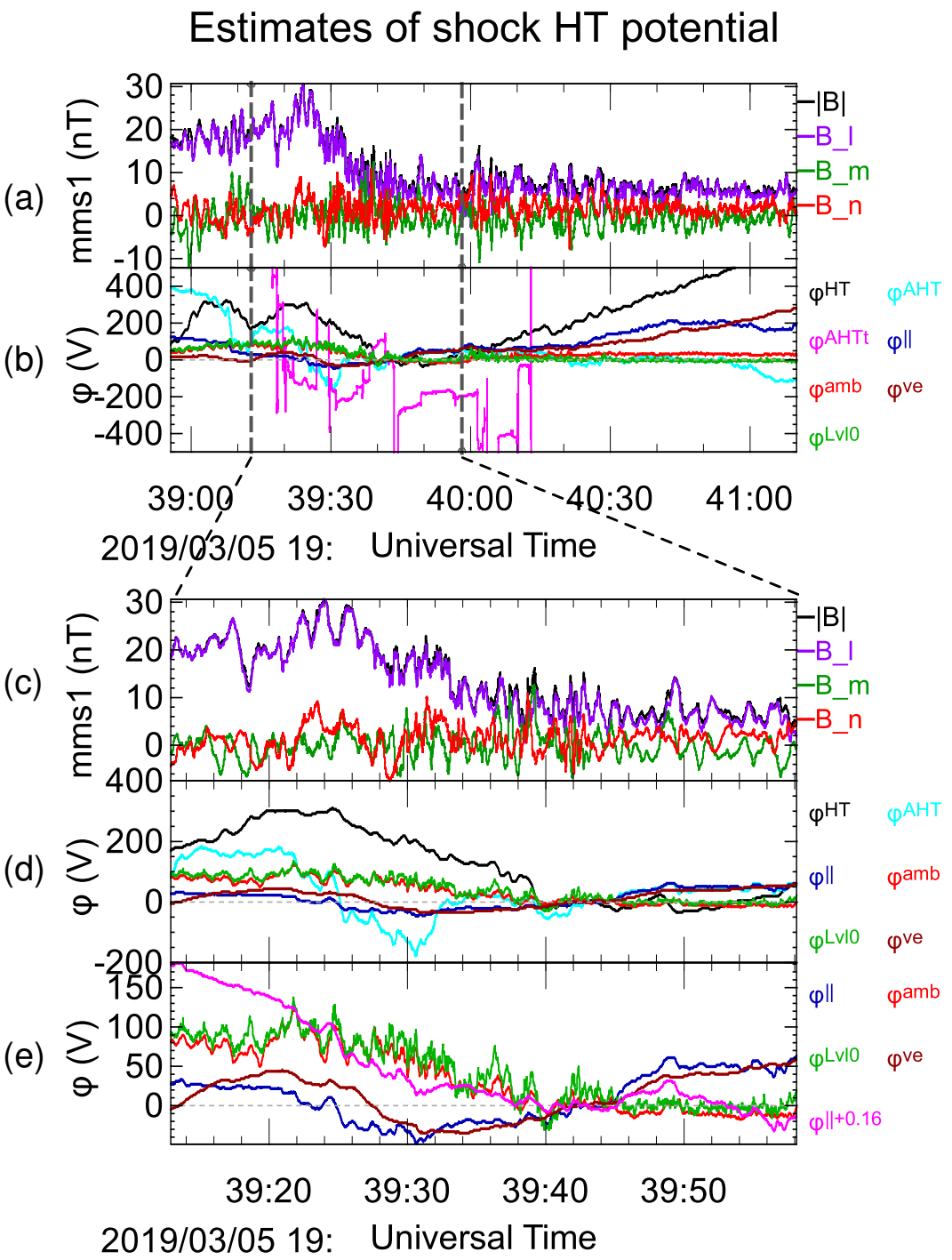

Figure 4. Comparison of different estimators for the HT potential profile through the shock shown in Figure 2, with the magnetic field for reference in panels (a) and (c) in shock normal *lmn* coordinates. Panel (b) plots all seven estimators enumerated in the preceding section. The bottom set of panels focuses on the region in the vicinity of the main shock ramp. Panel (e) includes a re-calculation (magenta) of $\phi^{\parallel}$after adding a constant offset of $+0.16\,\mathrm{mV/m}$ to $E_{\parallel}$. Note that all integrated potentials have employed integration constants to make the potentials zero at the base of the shock ramp, i.e., at 19:39:43.

infinite, the field is locally tangent to the shock surface, and the path along the field becomes infinite. These conditions cannot occur in strictly 1D simulations where B_n is constant in space and time. The extent of the variability in $B_n(t)$ can be seen in the red traces of Figure 4a,c.

The more conservative application of C&M's adaptive HT transformation results in ϕ^{AHT} (cyan). This treats B_n as constant, drawn from the undisturbed upstream environment. This clearly deviates from the strict objective of C&M's analysis, namely to make the tangential electric field vanish or, equivalently, to make the local electron bulk velocity aligned with the magnetic field. These remnant tangential fields could be the result of non-planarity (e.g. shock ripples Lowe and Burgess (2003); Johlander et al. (2016)), time dependence or both in more realistic 2D or 3D time-dependent shocks. Figure 4d shows that this ϕ^{AHT} (cyan) is larger in magnitude than the electron estimators, with a deep negative excursion within the shock ramp. The main potential change of $\sim 400\,\mathrm{V}$ is comparable to that in the classic constant V^{HT} approach (black) from Equation (12).

Two estimators do not involve directly a HT transformation, but instead work with estimators of $E_\parallel$. They either integrate $E_\parallel$ directly ($\phi^{\parallel}$ - blue) or effectively transform into the electron frame of reference (ϕ^{ve} - brown). Interestingly these two estimators agree with one another, demonstrating that the instrumental cross-calibrations are good and that the parallel component of the general **E** agrees well with the specialized $E_\parallel$ data product. Their main change through the steepest part of the shock ramp of $\sim 80\,\mathrm{V}$ is comparable to that found by the electron estimators ϕ^{amb} and ϕ^{Lvl0}. As shown in the magenta trace in Figure 4e, adding a constant offset of $0.16\,\mathrm{mV/m}$ to the experimental determination of $E_\parallel$ flattens the profile of $\phi^{\parallel}$ upstream of the shock and brings the potential profile into agreement with ϕ^{amb}. This same parallel offset would apply to ϕ^{ve}.

5 Discussion

The results of this work can be grouped into three categories of estimators for the HT potential profile across a shock:

Electron ambipolar (ϕ^{amb}) and kinetic (ϕ^{Lvl0}) estimators probe directly the electron pressure gradient source of the electric field in the HT frame via the electron fluid equation and its influence on the motion of individual electrons that traverse the shock via the Vlasov equation and Liouville's Theorem. These two estimators agree extremely well with one another in the MMS data presented here. Neither relies on details of the shock parameters or motion (with the exception of the normal direction for ϕ^{amb} as discussed below) nor transformation to a shock rest frame. This makes these estimators insensitive to knowledge of or errors in the shock and ambient plasma conditions.

The Liouville technique is powerful. It convolves details of the particle distribution over a restricted range of energies and phase space. It is the standard used by C&M, and historically. It does require assumptions about shock stationarity. However, deviations in the Liouville mapped vs. observed distributions can also provide indications of regions in phase space where waves or other processes must be playing significant roles in shaping or energizing electrons. For such applications, mapping a range of different pitch angles may be informative (Lefebvre et al., 2007) in separating the potential vs. non-stationary physics.

The ambipolar estimator requires good moments of the full electron distribution, and assumptions (which can be quantified) concerning the off-diagonal elements of $\underline{\underline{P}}_e$. Technically, it also requires determination of the shock normal. In practice, since the electron pressure is nearly isotropic, this is of secondary importance. Although this is

an integrated potential, it is the integral of a weighted time derivative and does not suffer the same kinds of drifts seen in electric field methods below.

The second group of estimators focus on extracting the parallel electric field via either its direct measurement (leading to $\phi^{\parallel}$) or a calculation of the electric field in the frame of the electron fluid (leading to ϕ^{ve}), essentially by evaluating the left hand side of the electron momentum equation (1). These two methods also agree well with one another. They do not immediately agree with the electron-only estimators ϕ^{amb} and ϕ^{Lvl0} although they do show a similar increase across the steepest portion of the shock ramp. It is also clear that there is a systematic drift in these potentials from the sloping nature of their upstream profiles in Figure 4b,e. This drift is likely the result of a baseline offset that was not fully corrected in calibration of $E_{\parallel}$; a constant offset addtional electric field would add a sloping line to the integrated potential. We added a constant $\Delta E_{\parallel} \sim +0.16\,\mathrm{mV/m}$, which is within the uncertainty of the baseline offset in $\mathbf{E}$ (see Section 2), to the parallel electric field. This flattened the resulting $\phi^{\parallel}$ potential profile immediately upstream and brought it closer within the main shock ramp to the two electron-based potentials, as demonstrated by the magenta trace in Figure 4e. We stress here that there is no a priori reason for the offset to be constant, especially in regions where the plasma conditions are changing.

For comparison to our ad hoc additon of a $0.16\,\mathrm{mV/m}$ offset, our inferred potential increase across the shock of $\sim$100 V occurs over a timescale of 20 s, corresponding to a distance of $\sim 150\,\mathrm{km}$. Thus the DC HT electric field is $\sim 0.7\,\mathrm{mV/m}$. This estimate reveals the challenges involved in relying on direct electric field measurements to determine the cross-shock HT potential in the face of much larger fluctuating fields and the uncertainties in field offsets. Our primary conclusion here is that in the absence of corroborating electron-based determinations of the potential, the field measurements on their own cannot provide an independent and accurate determination of the HT potential profile.

The third group of estimators involve transforms by a tangential velocity $\mathbf{V}^{T,\alpha}$ into an HT frame in which the tangential electric field vanishes. C&M have shown already that the traditional approach (cf our ϕ^{HT}), which makes the constant asymptotic upstream tangential field vanish, does not do a good job in the case of 1D time-dependent particle in cell simulations. Its shortcomings in the present work (ϕ^{HT}) are therefore not surprising. Their adaptive HT approach works well in their simulations, where the shock is strictly planar and the normal component B_n is constant. Applying their approach in this manner, with constant $B_n = B_n^{up}$, to real data shows that these assumptions do not work well in practice (ϕ^{AHT}). We have explored an extension of their work, to allow for the temporal variations of B_n, but not the direction of the normal vector $\mathbf{n}$ itself. That result (ϕ^{AHTt}) contains large jumps in ϕ that can be attributed to locations where $B_n(t)$ passes close to/through zero. Our discussion following the derivation of these adaptive forms in Section 3.6 anticipated the difficulties of the adaptive forms due to such locations and/or to the incomplete cancellation of the NIF motional electric field.

6 Conclusions

In this paper we have investigated methods for determining experimentally the electrostatic potential profile across collisionless shocks, concentrating on the contribution from the frame-invariant electric field parallel to the magnetic field. This potential is known as the deHoffmann-Teller (HT) potential since, in idealized 1D steady shocks it corresponds to that measured in the deHoffmann-Teller frame (de Hoffmann & Teller, 1950) in which the upstream, and downstream, flows are field-aligned and hence the $-\mathbf{V} \times \mathbf{B}$ motional electric field, which is the only field tangential to such

shocks, vanishes. We have exploited state-of-the-art in situ plasma and field data from the NASA MMS mission. Our results provide answers to two key questions:

In the case of non-ideal, temporally and spatially varying conditions, does the adaptive HT transform put forward by Comişel et al. (2015) and elaborated in Marghitu et al. (2017) offer the same improvements that it appears to do in 1D time-dependent particle in cell simulations? Irrespective of the quality of the electric field data, our analysis reveals short-comings of this adaptive approach that arise from the non-constant nature of the normal component of the magnetic field in 2D or 3D time-varying shocks. We explored further extensions of these adaptive ideas without success. There may be additional algorithms which could further extend this approach, but we are not aware of any.

Is it possible to measure particle and field parameters with sufficient accuracy to make reliable estimates of the integrated quasi-DC potential profile across collisionless shocks? Our results suggest a qualified "no" answer here. For some of our estimators, it is not possible to disentangle data quality/calibration issues from those related to assumptions of the various adaptive HT schemes. Algorithms that utilize a direct measure of the frame-invariant parallel electric field, either directly as a specialized data product or indirectly by transforming into the electron bulk flow frame (which requires high quality electron velocity-space moments), show variations with the right size and character, but superimposed on a larger scale DC component that may be attributable to small baseline offsets that remain after calibration. However, we would stress here the difficulties in calibrating DC field measurements in the highly variable conditions found in space, and also in particular across boundaries separating very different plasma conditions. In this sense, weaker interplanetary shocks, which take less time to go past the spacecraft and which have smaller changes in plasma parameters, provide more consistent fields measurements (Cohen et al., 2019).

We have used two standard methods as our prime measures of HT potentials. One used Liouville's theorem to map electron trajectories from the upstream to the downstream populations. This technique makes few demands on the particle and field measurements other than a consistent phase space calibration over a restricted range of energies and phase space densities, and the use of magnetic field data to determine the distribution in pitch angles. The field-aligned electrons are sufficient for this purpose, but the full pitch-angle space can also be employed (Lefebvre et al., 2007). The other method integrates the gradient in electron pressure, with some assumptions about gyrotropy and off-diagonal elements. These two methods are quite stable and agree quantitatively with one another. This agreement highlights the excellent quality of the MMS FPI data, although previous studies have been done many times with good success (Scudder, Mangeney, Lacombe, Harvey, Wu, & Anderson, 1986; Lefebvre et al., 2007; Cohen et al., 2019).

This work is based on the premise that the dominant influence on the electron phase space inflation at collisionless shocks is the result of electron interaction with DC shock fields. This idea, first put forward by Feldman et al. (1983) and then developed further (Scudder, Mangeney, Lacombe, Harvey, Wu, & Anderson, 1986) and applied (Schwartz et al., 1988; Lefebvre et al., 2007) (see Scudder (1995) for a review), is consistent with the reported electron beams seen within the shock transition and, e.g., the coherent reflection of ions at quasi-perpendicular shocks (Paschmann et al., 1982; Madanian et al., 2021). These processes point to the presence of coherent, DC fields.

We have assumed throughout that electrons remain magnetized through the shock layer. Typically this is a good assumption, although some crossings or substructures may violate this assumption (Schwartz et al., 2011; Balikhin et al., 1993; See et al., 2013).

It is clear that waves or other scattering processes are required to fill in voids left in electron velocity space (Scudder, Mangeney, Lacombe, Harvey, Wu, & Anderson, 1986) and to account for other distortions or features seen in the data. Shocks are known locations for a plethora of wave modes (K. A. Goodrich et al., 2018). Some work suggests that most if not all the electron phase space inflation, often referred to simply as heating, can be attributed to wave-particle interactions (Wilson et al., 2014; Stasiewicz & Eliasson, 2020) combined perhaps with magnetic pumping (Lichko & Egedal, 2020). Other work has concentrated on short-scale electrostatic structures within the shock transition (Chen et al., 2018). These structures are more amenable to direct DC field measurements, and may also be the building blocks of the overall shock profile, bridging the AC and DC worlds.

Future work will need to assemble all parts of this puzzle, which lies at the heart of the dynamics and energy partition at collisionless shocks. If electric field data on its own could be used to determine the HT potential profile with sufficient accuracy and certainty, mapping electron trajectories through that potential would point to regions in phase space where discrepancies would implicate specific electron-kinetic wave modes, nonlinear structures or other physical processes by their kinetic signatures. Our conclusion that direct integration of the measured electric fields is difficult to achieve with the necessary certainty nonetheless points to the need to examine fine details of the electron phase space distributions themselves for clues to help address this problem.

Acknowledgments

ARTEMIS and Wind data were drawn from the SPDF/CDAWEB repository (`https://cdaweb.gsfc.nasa.gov/index.html/`). We gratefully acknowledge the respective instrument teams and archive curators. We are grateful to one of the reviewers for their detailed positive suggestions, and to Octav Marghitu for helpful comments on an earlier draft. MMS data can be found at the MMS public Science Data Center (`https://lasp.colorado.edu/mms/sdc/public/`). All the data analysis and graphics were performed using the opensource QSAS Science Analysis System (`https://sourceforge.net/projects/qsas/`). Several of us are grateful to ISSI, Bern, for their support of a Working Team. This work was supported by NASA Award 80NSSC19K0849 together with NASA MMS contracts to the instrument teams. IG is supported by a Royal Society URF.

References

Angelopoulos, V. (2010). The ARTEMIS mission. In *The ARTEMIS mission* (pp. 3–25). Springer New York. Retrieved from `https://doi.org/10.1007/978-1-4614-9554-3_2` doi: 10.1007/978-1-4614-9554-3_2

Balikhin, M., Gedalin, M., & Petrukovich, A. (1993, March). New mechanism for electron heating in shocks. *Phys. Rev. Lett.*, *70*(9), 1259-1262. doi: 10.1103/PhysRevLett.70.1259

Burch, J. L., Moore, T. E., Torbert, R. B., & Giles, B. L. (2016, March). Magnetospheric Multiscale Overview and Science Objectives. *Space Sci. Rev.*, *199*, 5-21. doi: 10.1007/s11214-015-0164-9

Burgess, D., & Scholer, M. (2015). *Collisionless Shocks in Space Plasmas*. Cambridge University Press.

Chen, L. J., Wang, S., Wilson, L. B., Schwartz, S., Bessho, N., Moore, T., ... Avanov, L. (2018, June). Electron Bulk Acceleration and Thermalization at Earth's Quasiperpendicular Bow Shock. *Phys. Rev. Lett.*, *120*(22), 225101. doi: 10.1103/PhysRevLett.120.225101

Cohen, I. J., Schwartz, S. J., Goodrich, K. A., Ahmadi, N., Ergun, R. E., Fuselier, S. A., ... Burch, J. L. (2019, June). High-Resolution Measurements

of the Cross-Shock Potential, Ion Reflection, and Electron Heating at an Interplanetary Shock by MMS. *J. Geophys. Res.*, *124*(6), 3961-3978. doi: 10.1029/2018JA026197

Comișel, H., Narita, Y., & Motschmann, U. (2015, March). Adaptation of the de Hoffmann-Teller frame for quasi-perpendicular collisionless shocks. *Ann. Geophys.*, *33*(3), 345-350. doi: 10.5194/angeo-33-345-2015

de Hoffmann, F., & Teller, E. (1950, November). Magneto-Hydrodynamic Shocks. *Phys. Rev.*, *80*(4), 692-703. doi: 10.1103/PhysRev.80.692

Dimmock, A. P., Balikhin, M. A., Krasnoselskikh, V. V., Walker, S. N., Bale, S. D., & Hobara, Y. (2012, February). A statistical study of the cross-shock electric potential at low Mach number, quasi-perpendicular bow shock crossings using Cluster data. *J. Geophys. Res.*, *117*(A2), A02210. doi: 10.1029/2011JA017089

Ergun, R. E., Tucker, S., Westfall, J., Goodrich, K. A., Malaspina, D. M., Summers, D., ... Cully, C. M. (2016, March). The Axial Double Probe and Fields Signal Processing for the MMS Mission. *Space Sci. Rev.*, *199*, 167-188. doi: 10.1007/s11214-014-0115-x

Feldman, W. C., Anderson, R. C., Bame, S. J., Gary, S. P., Gosling, J. T., McComas, D. J., ... Hoppe, M. M. (1983, Jan). Electron velocity distributions near the earth's bow shock. *J. Geophys. Res.*, *88*(A1), 96-110. doi: 10.1029/JA088iA01p00096

Goodrich, C. C., & Scudder, J. D. (1984, August). The adiabatic energy change of plasma electrons and the frame dependence of the cross-shock potential at collisionless magnetosonic shock waves. *J. Geophys. Res.*, *89*(A8), 6654-6662. doi: 10.1029/JA089iA08p06654

Goodrich, K. A., Ergun, R., Schwartz, S. J., Wilson, L. B., Newman, D., Wilder, F. D., ... Andersson, L. (2018, November). MMS Observations of Electrostatic Waves in an Oblique Shock Crossing. *J. Geophys. Res.*, *123*(11), 9430-9442. doi: 10.1029/2018JA025830

Hanson, E. L. M., Agapitov, O. V., Mozer, F. S., Krasnoselskikh, V., Bale, S. D., Avanov, L., ... Giles, B. (2019, March). Cross-Shock Potential in Rippled Versus Planar Quasi-Perpendicular Shocks Observed by MMS. *Geophys. Res. Lett.*, *46*(5), 2381-2389. doi: 10.1029/2018GL080240

Harten, R., & Clark, K. (1995, February). The Design Features of the GGS Wind and Polar Spacecraft. *Sp. Sci. Rev.*, *71*(1-4), 23-40. doi: 10.1007/BF00751324

Johlander, A., Schwartz, S. J., Vaivads, A., Khotyaintsev, Y. V., Gingell, I., Peng, I. B., ... Burch, J. L. (2016, October). Rippled Quasiperpendicular Shock Observed by the Magnetospheric Multiscale Spacecraft. *Phys. Rev. Lett.*, *117*(16), 165101. doi: 10.1103/PhysRevLett.117.165101

Khrabrov, A. V., & Sonnerup, B. U. Ö. (1998, January). DeHoffmann-Teller Analysis. *ISSI Scientific Reports Series*, *1*, 221-248.

Krasnoselskikh, V., Balikhin, M., Walker, S. N., Schwartz, S. J., Sundkvist, D., Lobzin, V., ... Comisel, H. (2013, October). The Dynamic Quasiperpendicular Shock: Cluster Discoveries. *Sp. Sci. Rev.*, *178*(2-4), 535-598. doi: 10.1007/s11214-013-9972-y

Kucharek, H., Möbius, E., Li, W., Farrugia, C. J., Popecki, M. A., Galvin, A. B., ... Bochsler, P. A. (2003, October). On the source and acceleration of energetic He^+: A long-term observation with ACE/SEPICA. *J. Geophys. Res.*, *108*(A10), 8040. doi: 10.1029/2003JA009938

Lefebvre, B., Schwartz, S. J., Fazakerley, A. F., & Décréau, P. (2007, September). Electron dynamics and cross-shock potential at the quasi-perpendicular Earth's bow shock. *J. Geophys. Res.*, *112*(A9), A09212. doi: 10.1029/2007JA012277

Lichko, E., & Egedal, J. (2020, June). Magnetic pumping model for energizing superthermal particles applied to observations of the Earth's bow shock. *Nat.*

Commun., *11*, 2942. doi: 10.1038/s41467-020-16660-4

Lindqvist, P.-A., Olsson, G., Torbert, R. B., King, B., Granoff, M., Rau, D., ... Tucker, S. (2016, March). The Spin-Plane Double Probe Electric Field Instrument for MMS. *Space Sci. Rev.*, *199*, 137-165. doi: 10.1007/s11214-014-0116-9

Lowe, R. E., & Burgess, D. (2003, March). The properties and causes of rippling in quasi-perpendicular collisionless shock fronts. *Ann. Geophys.*, *21*(3), 671-679. doi: 10.5194/angeo-21-671-2003

Madanian, H., Desai, M. I., Schwartz, S. J., Wilson, I., L. B., Fuselier, S. A., Burch, J. L., ... Lindqvist, P. A. (2021, February). The Dynamics of a High Mach Number Quasi-perpendicular Shock: MMS Observations. *Astrophys. J.*, *908*(1), 40. doi: 10.3847/1538-4357/abcb88

Marghitu, O., Comișel, H., & Scholer, M. (2017, July). On the nonstationarity of collisionless shocks and its impact on deriving the cross-shock potential. *Geophys. Res. Lett.*, *44*(13), 6500-6507. doi: 10.1002/2017GL073241

Mitchell, J. J., & Schwartz, S. J. (2013, Dec). Nonlocal electron heating at the Earth's bow shock and the role of the magnetically tangent point. *J. Geophys. Res.*, *118*(12), 7566-7575. doi: 10.1002/2013JA019226

Mitchell, J. J., & Schwartz, S. J. (2014, February). Isothermal magnetosheath electrons due to nonlocal electron cross talk. *J. Geophys. Res.*, *119*(2), 1080-1093. doi: 10.1002/2013JA019211

Paschmann, G., Haaland, S. E., Phan, T. D., Sonnerup, B. U. Ö., Burch, J. L., Torbert, R. B., ... Fuselier, S. A. (2018, March). Large-Scale Survey of the Structure of the Dayside Magnetopause by MMS. *J. Geophys. Res.*, *123*(3), 2018-2033. doi: 10.1002/2017JA025121

Paschmann, G., Sckopke, N., Bame, S. J., & Gosling, J. T. (1982, August). Observations of gyrating ions in the foot of the nearly perpendicular bow shock. *Geophys. Res. Lett.*, *9*(8), 881-884. doi: 10.1029/GL009i008p00881

Pollock, C., Moore, T., Jacques, A., Burch, J., Gliese, U., Saito, Y., ... others (2016, March). Fast Plasma Investigation for Magnetospheric Multiscale. *Space Sci. Rev.*, *199*, 331-406. doi: 10.1007/s11214-016-0245-4

Russell, C. T., Anderson, B. J., Baumjohann, W., Bromund, K. R., Dearborn, D., Fischer, D., ... Richter, I. (2016, March). The Magnetospheric Multiscale Magnetometers. *Space Sci. Rev.*, *199*, 189-256. doi: 10.1007/s11214-014-0057-3

Schwartz, S. J. (1998, January). Shock and Discontinuity Normals, Mach Numbers, and Related Parameters. *ISSI Scientific Reports Series*, *1*, 249-270.

Schwartz, S. J. (2006, June). Shocks: Commonalities in Solar-Terrestrial Chains. *Sp. Sci. Rev.*, *124*(1-4), 333-344. doi: 10.1007/s11214-006-9093-y

Schwartz, S. J., Henley, E., Mitchell, J., & Krasnoselskikh, V. (2011, November). Electron Temperature Gradient Scale at Collisionless Shocks. *Phys. Rev. Lett.*, *107*(21), 215002. doi: 10.1103/PhysRevLett.107.215002

Schwartz, S. J., Thomsen, M. F., Bame, S. J., & Stansberry, J. (1988, November). Electron heating and the potential jump across fast mode shocks. *J. Geophys. Res.*, *93*, 12923-12931. doi: 10.1029/JA093iA11p12923

Schwartz, S. J., Thomsen, M. F., & Gosling, J. T. (1983, March). Ions upstream of the earth's bow shock: A theoretical comparison of alternative source populations. *J. Geophys. Res.*, *88*(A3), 2039-2047. doi: 10.1029/JA088iA03p02039

Schwartz, S. J., Zweibel, E. G., & Goldman, M. (2013, October). Microphysics in Astrophysical Plasmas. *Sp. Sci. Rev.*, *178*(2-4), 81-99. doi: 10.1007/s11214-013-9975-8

Scudder, J. D. (1987, December). The field-aligned flow approximation for electrons within layers possessing a normal mass flux: A corollary to the deHoffmann-Teller theorem. *J. Geophys. Res.*, *92*(A12), 13447-13455. doi: 10.1029/JA092iA12p13447

Scudder, J. D. (1995, February). A review of the physics of electron heating at collisionless shocks. *Adv. Space Res.*, *15*(8-9), 181-223. doi: 10.1016/0273-1177(94)00101-6

Scudder, J. D., Mangeney, A., Lacombe, C., Harvey, C. C., Aggson, T. L., Anderson, R. R., ... Russell, C. T. (1986, October). The resolved layer of a collisionless, high β, supercritical, quasi-perpendicular shock wave 1. Rankine-Hugoniot geometry, currents, and stationarity. *J. Geophys. Res.*, *91*(A10), 11019-11052. doi: 10.1029/JA091iA10p11019

Scudder, J. D., Mangeney, A., Lacombe, C., Harvey, C. C., Wu, C. S., & Anderson, R. R. (1986, October). The resolved layer of a collisionless, high β, supercritical, quasi-perpendicular shock wave, 3. Vlasov electrodynamics. *J. Geophys. Res.*, *91*(A10), 11075-11098. doi: 10.1029/JA091iA10p11075

See, V., Cameron, R. F., & Schwartz, S. J. (2013, April). Non-adiabatic electron behaviour due to short-scale electric field structures at collisionless shock waves. *Ann. Geophys.*, *31*(4), 639-646. doi: 10.5194/angeo-31-639-2013

Slavin, J. A., & Holzer, R. E. (1981, December). Solar wind flow about the terrestrial planets, 1. Modeling bow shock position and shape. *J. Geophys. Res.*, *86*(A13), 11401-11418. doi: 10.1029/JA086iA13p11401

Sonnerup, B. U. Ö. (1969, January). Acceleration of particles reflected at a shock front. *J. Geophys. Res.*, *74*(5), 1301. doi: 10.1029/JA074i005p01301

Stasiewicz, K., & Eliasson, B. (2020, November). Quasi-adiabatic and Stochastic Heating and Particle Acceleration at Quasi-perpendicular Shocks. *Astrophys. J.*, *903*(1), 57. doi: 10.3847/1538-4357/abb825

Stone, R. G., & Tsurutani, B. T. (1985, January). Collisionless shocks in the heliosphere. A tutorial review. *Washington DC American Geophysical Union Geophysical Monograph Series*, *34*. doi: 10.1029/GM034

Thomsen, M. F., Gosling, J. T., Bame, S. J., Quest, K. B., Winske, D., Livesey, W. A., & Russell, C. T. (1987, March). On the noncoplanarity of the magnetic field within a fast collisionless shock. *J. Geophys. Res.*, *92*(A3), 2305-2314. doi: 10.1029/JA092iA03p02305

Thomsen, M. F., Mellott, M. M., Stansberry, J. A., Bame, S. J., Gosling, J. T., & Russell, C. T. (1987, September). Strong electron heating at the Earth's bow shock. *J. Geophys. Res.*, *92*(A9), 10119-10124. doi: 10.1029/JA092iA09p10119

Thomsen, M. F., Schwartz, S. J., & Gosling, J. T. (1983, October). Observational evidence on the origin of ions upstream of the earth's bow shock. *J. Geophys. Res.*, *88*(A10), 7843-7852. doi: 10.1029/JA088iA10p07843

Torbert, R. B., Russell, C. T., Magnes, W., Ergun, R. E., Lindqvist, P.-A., LeContel, O., ... Lappalainen, K. (2016, March). The FIELDS Instrument Suite on MMS: Scientific Objectives, Measurements, and Data Products. *Space Sci. Rev.*, *199*, 105-135. doi: 10.1007/s11214-014-0109-8

Tsurutani, B. T., & Stone, R. G. (1985, January). Collisionless shocks in the heliosphere: Reviews of current research. *Washington DC American Geophysical Union Geophysical Monograph Series*, *35*. doi: 10.1029/GM035

Wilson, L. B., Brosius, A. L., Gopalswamy, N., Nieves-Chinchilla, T., Szabo, A., Hurley, K., ... TenBarge, J. M. (2021, June). A quarter century of wind spacecraft discoveries. *Reviews of Geophysics*, *59*(2), e2020RG000714. doi: 10.1029/2020rg000714

Wilson, L. B., Chen, L.-J., & Roytershteyn, V. (2021, January). The discrepancy between simulation and observation of electric fields in collisionless shocks. *Frontiers in Astronomy and Space Sciences*, *7*, 97. doi: 10.3389/fspas.2020.592634

Wilson, L. B., Sibeck, D. G., Breneman, A. W., Le Contel, O., Cully, C., Turner, D. L., ... Malaspina, D. M. (2014, August). Quantified energy dissipation rates in the terrestrial bow shock: 2. Waves and dissipation. *J. Geophys. Res.*, *119*(8), 6475-6495. doi: 10.1002/2014JA019930

Wu, C. S. (1984, October). A fast Fermi process: Energetic electrons accelerated by a nearly perpendicular bow shock. *J. Geophys. Res.*, *89*(A10), 8857-8862. doi: 10.1029/JA089iA10p08857